Multi-Phase Sputtered TiO$_2$-Induced Current–Voltage Distortion in Sb$_2$Se$_3$ Solar Cells

Christopher H. Don,* Thomas P. Shalvey, Matthew J. Smiles, Luke Thomas, Laurie J. Phillips, Theodore D. C. Hobson, Harry Finch, Leanne A. H. Jones, Jack E. N. Swallow, Nicole Fleck, Christopher Markwell, Pardeep K. Thakur, Tien-Lin Lee, Deepnarayan Biswas, Leon Bowen, Benjamin A. D. Williamson, David O. Scanlon, Vinod R. Dhanak, Ken Durose, Tim D. Veal, and Jonathan D. Major

Despite the recent success of CdS/Sb$_2$Se$_3$ heterojunction devices, cadmium toxicity, parasitic absorption from the relatively narrow CdS band gap (2.4 eV) and multiple reports of inter-diffusion at the interface forming Cd(S,Se) and Sb$_2$(S,Se)$_3$ phases, present significant limitations to this device architecture. Among the options for alternative partner layers in antimony chalcogenide solar cells, the wide band gap, non-toxic titanium dioxide (TiO$_2$) has demonstrated the most promise. It is generally accepted that the anatase phase of the polymorphic TiO$_2$ is preferred, although there is currently an absence of analysis with regard to phase influence on device performance. This work reports approaches to distinguish between TiO$_2$ phases using both surface and bulk characterization methods. A device fabricated with a radio frequency (RF) magnetron sputtered rutile-TiO$_2$ window layer (FTO/TiO$_2$/Sb$_2$Se$_3$/P3HT/Au) achieved an efficiency of 6.88% and near-record short–circuit current density (J_{sc}) of 32.44 mA cm^{-2}, which is comparable to established solution based TiO$_2$ fabrication methods that produced a highly anatase-TiO$_2$ partner layer and a 6.91% efficiency device. The sputtered method introduces reproducibility challenges via the enhancement of interfacial charge barriers in multi-phase TiO$_2$ films with a rutile surface and anatase bulk. This is shown to introduce severe S-shaped current–voltage (J–V) distortion and a drastic fill–factor (FF reduction in these devices.

1. Introduction

Antimony selenide (Sb$_2$Se$_3$) has rapidly risen to prominence as a candidate material for application as an absorber layer, primarily in thin-film photovoltaic (PV) solar cell devices, but also for photodetectors and photoelectrochemical water splitting.[1–5] In addition to this material's favorable combination of properties; boasting a nearly ideal 1.18 eV band gap,[6] high absorption coefficient,[7–9] low toxicity and high stability,[10–12] Sb$_2$Se$_3$ has further demonstrated a high degree of versatility. It is capable of being deposited in both substrate[13–17] and superstrate[18–26] geometries and with a wide variety of deposition techniques; from low temperature solution-based methods,[21,24–26] to high temperature physical vapor deposition approaches.[13–15,18–20,22,23] This has led to a rapid improvement in performance with a record power conversion efficiency (PCE) of 10.6%

C. H. Don, T. P. Shalvey, M. J. Smiles, L. Thomas, L. J. Phillips,
T. D. C. Hobson, H. Finch, V. R. Dhanak, K. Durose, T. D. Veal, J. D. Major
Stephenson Institute for Renewable Energy
Department of Physics
University of Liverpool
Liverpool L69 7ZF, UK
E-mail: C.H.Don@liverpool.ac.uk

L. A. H. Jones, J. E. N. Swallow
Department of Materials
University of Oxford
Parks Road, Oxford OX1 3PH, UK

N. Fleck, C. Markwell
Department of Mathematics, Physics, and Electrical Engineering
Northumbria University
Newcastle upon Tyne NE1 8QH, UK

P. K. Thakur, T.-L. Lee, D. Biswas
UK Diamond Light Source Ltd, Diamond House
Harwell Science and Innovation Campus
Didcot Oxfordshire OX11 0DE, UK

L. Bowen
Department of Physics
University of Durham
Durham DH1 3LE, UK

ADVANCED
SCIENCE NEWS

www.advancedsciencenews.com

ADVANCED
MATERIALS
INTERFACES

www.advmatinterfaces.de

for the pure selenide composite[25] and 10.7% for the $Sb_2(S,Se)_3$ alloy.[26]

The majority of reported Sb_2Se_3 device work utilizes CdS as the junction partner layer—a device architecture inherited from established inorganic thin film technologies such as CdTe and CIGS.[27,28] $CdS/Sb_2(S,Se)_3$ junction devices are thus adopted by many groups and have been widely successful.[15–17,25,26,29,30] Current antimony chalcogenide research largely focuses on grain orientation of its characteristic 'one–dimensional'(1D) nanoribbon structure[31–34] and sulfurization/selenization methods to reduce anion site vacancy defects ($V_{S,Se}$).[15,35,36] Whilst this has proved a successful optimization approach and has helped to reduce the open–circuit voltage (V_{oc}) deficit in $Sb_2(S,Se)_3$ devices,[11,16,37,38] the reliance on a CdS window layer is restrictive. The band gap of 2.4 eV is sub-optimal for a window layer leading to parasitic absorption losses,[39,40] whilst the inclusion of cadmium increases the overall toxicity. The CdS/Sb_2Se_3 heterojunction is also prone to inter-diffusion, leading to the unintended formation of $Cd(Se,S)$ and $Sb_2(S,Se)_3$ phases at the near interface - primarily associated with superstrate oriented devices,[40,41] but also evident in substrate geometries.[13,16]

Alternative junction partner layers employed include wide band gap, non-toxic metal oxides such as; SnO_2, ZnO, and TiO_2, which have achieved 4.03%, 5.93% and 7.62% *PCE*, respectively.[31,42,43] A study on interfacial properties of different Sb_2Se_3 heterojunctions by Lu et al. found that transition layers formed from intermixing for both ZnO/Sb_2Se_3 and CdS/Sb_2Se_3 junctions, whilst the TiO_2/Sb_2Se_3 layers remained discrete due to the high stability of TiO_2.[44] Devices with metal oxide partner layers typically use superstrate device orientation due to the high temperature crystallization anneal needed, which would degrade absorber quality in a substrate architecture. It is our belief that changing the surface on which Sb_2Se_3 is grown (the partner layer in superstrate devices) is impeding progress in device performance due to constant re-optimization of subsequent absorber layer deposition conditions to achieve ideal ribbon orientation.[32,45] In this regard, groups already employing either substrate architecture or a CdS partner layer in superstrate, will be resistant to experimentation of new interfacing materials due to the requirement for re-optimization of the entire device stack. This is highlighted by our previous work whereby Sb_2Se_3 devices fabricated with CdS window layers in our setup performed considerably worse than the TiO_2/Sb_2Se_3 devices.[40]

Interest in $Sb_2(S,Se)_3$ for PVinitially started as a progression of organic and dye-sensitized solar cells, which traditionally employed mesoporous and later planar TiO_2 window layers.[46–49] This work has led to the promising results achieved with TiO_2partner layers for both Sb_2S_3 (7.5% *PCE*)[50] and Sb_2Se_3 (7.6% *PCE*).[31] Whilst both of these devices employed spray pyrolysis of their initial blocking layer, followed by a 450 °C an-

neal, the chemical bath deposition (CBD) deposited Sb_2S_3 device additionally utilized mesoporous TiO_2 for their 'sensitized' interface, which is clearly unsuitable for physical vapour deposition (PVD) grown absorber material. Fabrication approaches for TiO_2 entirely focus on solution based methods (sol–gel, spin-cast, spray pyrolysis), with very similar precursor preparation, followed by a post-depostion annealing step <500 °C.[20,31,45,49–51] It is typically assumed that the anatase phase (a-TiO_2) of the polymorphic TiO_2 is attained through this method, since the irreversible anatase-rutile phase transition is commonly reported to be >600 °C. Despite this, there are numerous reports of the rutile phase (r-TiO_2) being produced at lower processing temperatures and there is generally a lack of rigorous analysis of how the phase of TiO_2 may influence the device performance. Detailed discussion on the anatase-rutile transition is beyond the scope of this manuscript, but can be found elsewhere.[52] Recent optimization efforts favor post-deposition treatments of TiO_2 layers to improve interfacial properties and alignment of the conduction bands,[53–55] although it is not clear to what extent this effect is entangled with $Sb_2(S,Se)_3$ growth improvement.

Previously, our group has employed a solution-based deposition method to fabricate planar TiO_2 films. This method has been highly reproducible and delivered $FTO/TiO_2/Sb_2Se_3/Au$ devices in excess of 7% *PCE*.[20] The solution process is time consuming, wasteful and results in thickness variations producing contact non-uniformity across the substrate. In contrast, the sputtering process offers the potential for far greater experimental throughput and is proven to be industrial scalable, although radio frequency (RF) sputtering of TiO_2 is much less widely implemented for PV applications.

In this work, we compare TiO_2/Sb_2Se_3 junction solar cell devices fabricated with established spin-cast solution deposited and experimentalRF magnetron sputtered TiO_2 window layers. We propose suitable methods of polymorphic TiO_2 phase characterization in the context of implementation as a partner layer and the ramifications of phase on both the front contact and antimony selenide band alignment. Variable performance from devices fabricated with the sputtered TiO_2 partner layer was observed and attributed to multi-phase TiO_2 films which cause severe 'S-shaped' 'kinks' in the illuminated current–voltage measurements. We believe this result highlights the importance of phase control in TiO_2 partner layer preparation for application in $Sb_2(S,Se)_3$ solar cells (which is sometimes overlooked) and provides a pathway for an easier transition from $CdS/Sb_2(S,Se)_3$ to $TiO_2/Sb_2(S,Se)_3$ device structures. The high performance capability of scalable RF magnetron sputtered TiO_2 window layers for Sb_2Se_3 solar cell devices is demonstrated despite considerable short-circuit current (J_{sc}) loss due to an interfacial barrier inhibiting charge extraction under illumination. The $FTO/TiO_2/Sb_2Se_3/P3HT/Au$ device achieved a *PCE* of 6.88%, and J_{sc} of 32.44 mA cm^{-2}.

2. Experimental Section

2.1. Device Fabrication

All devices in this work were fabricated with an $FTO/TiO_2/Sb_2Se_3/P3HT/Au$ architecture in superstrate orientation. Commercially available TEC15 glass from NSG Ltd. was used as the substrate and front contact which comprises

B. A. D. Williamson
Department of Materials Science and Engineering
Norwegian University of Science and Technology (NTNU)
Trondheim 7491, Norway
D. O. Scanlon
Department of Chemistry
University College London
20 Gordon Street, London WC1H 0AJ, UK

**ADVANCED
SCIENCE NEWS**

www.advancedsciencenews.com

**ADVANCED
MATERIALS
INTERFACES**
Open Access

www.advmatinterfaces.de

SnO_2:F (FTO)-coated soda-lime glass. Prior to deposition, the substrate was cleaned using acetone, isopropyl alcohol, and deionized water; followed by a 10 min ultraviolet (UV) ozone treatment. TiO_2 films were then deposited onto the clean FTO substrates via either spin-casting solution (sol-TiO_2) or RF magnetron sputtering (sp-TiO_2). The sol-TiO_2 films were deposited by sequentially spin-casting two 275 μl doses of a 0.3 M concentration of titanium isopropoxide (TTIP) in ethyl alcohol solution within a nitrogen atmosphere at 3000 rpm, with a 10 min 120 °C hot plate anneal after each dose to drive off any remaining solvent.[56] Spin-cast sol-TiO_2 films were then annealed post-deposition at 500 °C for 30 min in air.

TiO_2 films (70 nm thick) were sputtered at 3.29 W cm^{-2} onto the FTO substrates from a TiO_2 target (99.95% purity, Pi-Kem Ltd.) at room temperature in a 3 mTorr pressure argon atmosphere with 1% reactive O_2 incorporated to ensure a stoichiometric film without oxygen deficiency. Sputtered films then underwent post-deposition annealing in an identical process to the reference sol-TiO_2 device.

After a 10 min UV ozone clean of the TiO_2, Sb_2Se_3 (Alfa Aesar 5N granulate) was deposited onto the TiO_2 surface via the two-step close-space sublimation (CSS) process outlined by Hutter et al.[57] For the standard process, an initial seed layer was deposited with source and substrate temperatures of 440 and 350 °C respectively at vacuum for 15 min, followed by a growth phase at 530 and 480 °C at 10 Torr for an additional 15 min to deliver a ≈1.2 μm thick film. For deposition on to the sputtered TiO_2, the substrate temperature is required to be increased from 350 to 400 °C, as discussed in the approaching Section 3.1. Following the absorber deposition, a 5 mg ml^{-1} solution of P3HT in chlorobenzene (100–360 nm) was then deposited on to the Sb_2Se_3 back surface via spin-casting as both a hole transporter layer (HTL) and to act as a pinhole blocker.[58] Finally, 50 nm thick 0.1 cm^2 gold contacts were deposited on to the back surface via thermal evaporation.

2.2. Material Characterization

Scanning electron microscopy (SEM) was obtained using a Carl Zeiss 300 VP Scanning Electron microscope. Operated in variable pressure mode as devices were uncoated. Images were mounted cross-sectionally, and images taken in BSE (Backscattered electron imaging mode). Cross-section was prepared by encapsuling the device with epoxy resin and a silicon wafer cap. A Hitachi E-3500 Ion mill system operated at 6 keV for 6 h was used to prepare a cross-section area for imaging and chemical analysis. Transmission electron microscopy (TEM) was carried out using JEOL 2100F TEM operated at 200 keV. TEM lamellar, were prepared using FEI Helios MK2 NanoLab 600 DualBeam. Atomic force microscopy (AFM) topographic images were acquired using a commercial AFM system (Veeco DI3100, Bruker Corporation). Intermittent contact mode imaging techniques were applied using a cantilever with a stiffness of 26 N/m and tip radius of <7 nm (OTESPA, Apex Probes). X-ray diffraction (XRD) θ-2θ measurements were taken using a Rigaku SmartLab diffractometer with a Cu rotating anode (λ = 1.542 Å) and a Ge(220) × 2 monochromator in parallel beam configuration. For grazing incidence, Ge(220) × 2 monochromator was replaced with IPS + PSA

slits, with an incident angle between 0.6 ° and 1.0 °. Current density–voltage (J–V) measurements were taken using a TS Space Systems solar simulator (class AAA) calibrated to AM1.5G. External quantum efficiency (EQE) measurements were taken with a Bentham PVE300 system. Raman spectra were obtained with a Renishaw InVia system with a 532 nm green laser for two accumulations of 6 s acquisition at 10 mW. Raman band positions were calibrated to the 520 cm^{-1} silicon peak with a resolution of 1 cm^{-1}. X-ray photoelectron spectroscopy (XPS) spectra of reference TiO_2 films and FTO for the purpose of determining band positions was measured using a monochromated Al Kα (hν = 1486.6 eV) X-ray source and a PSP Vacuum Technology hemispherical electron-energy analyzer at the University of Liverpool. Values for sol-TiO_2 and Sb_2Se_3 films are recreated with permission from Shiel et al.[59] Energy calibration was performed by measuring the Fermi edge and $3d_{5/2}$ core-level position of a polycrystalline silver foil Ar$^+$ sputtered clean under vacuum (more detail here[60]). The precision of binding energy determination is ±0.1 eV, which when added in quadrature for VBM and SEC positions, gives an uncertainty of ±0.14 eV on calculated band positions. Additional photoemission measurements were obtained at the i09 beamline of the Diamond Light Source facility for soft X-ray energies of 800 eV (70 eV pass energy, 50 meV step size) with analyser mode "Angular45" and 1090 eV (100 eV pass energy, 50 meV step size) with analyser mode "Angular56". Transmission and reflectance measurements were taken using a Shimadzu SolidSpec-3700 UV–vis spectrophotometer between 250 and 1500 nm. Indirect band gaps were then extracted via the Tauc method.

2.3. Computational Methods

Theoretical calculations were performed using plane-wave periodic density functional theory (DFT) within the Vienna ab-initio Simulation Package (VASP).[61–64] The HSE06[65] (Heyd–Scuseria–Ernzerhof) hybrid functional was used to treat the exchange and correlation, and the projector-augmented wave (PAW) method[66] described the interactions between the core (Ti:[Ar] and O[He]) and the valence electrons. HSE06 and hybrid functionals in general, are known to consistently give accurate results compared to experiment[67–70] particularly toward the electronic structure of anatase and rutile TiO_2.[71–74] Geometry optimizations of both anatase and rutile were carried out prior to calculating the density-of-states (DoS) using a plane-wave energy cut-off of 700 eV and Γ-centred k-point meshes of 7 × 7 × 5 and 5 × 5 × 8 respectively. Convergence was deemed complete when the maximum force on any ion was less than 0.01 eV Å^{-1}.
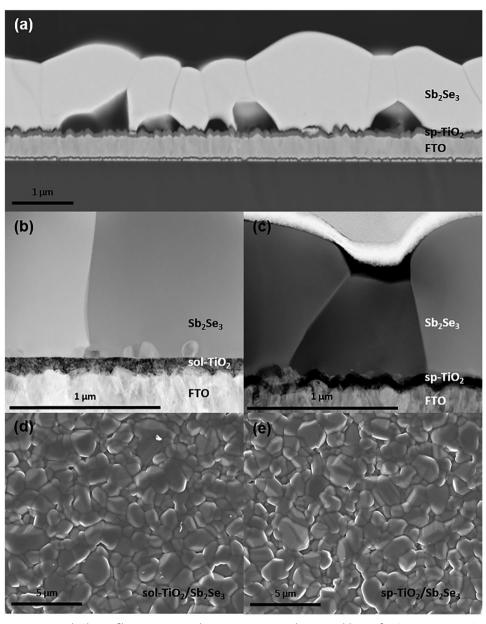
3. Results and Discussion

3.1. CSS Re-Optimization for sp-TiO_2

Whilst the CSS process had previously been optimized for deposition on the established sol-TiO_2 films,[20,40,57] the same Sb_2Se_3 film quality was not reproduced upon replacement of the sol-TiO_2 surface with sp-TiO_2. This is not necessarily unsurprising, given the substrate dependence of Sb_2Se_3 grain morphology and orientation,[32,45] but this is perhaps the first report

**ADVANCED
SCIENCE NEWS**

www.advancedsciencenews.com

**ADVANCED
MATERIALS
INTERFACES**

www.advmatinterfaces.de

Figure 1. Device cross-sections with Sb_2Se_3 film grown at a substrate temperature during seed layer of 350 °C on a) sp-TiO_2 obtained with back-scattered electron SEM and b) sol-TiO_2 obtained with dark-field TEM. c) Dark-field TEM device cross-section for Sb_2Se_3 grown on sp-TiO_2 with a substrate temperature during seed layer of 400 °C. Surface secondary electron SEM images of Sb_2Se_3 grain structure grown on d) sol-TiO_2 and e) sp-TiO_2 at 350 and 400 °C, respectively.

of surface roughness affecting absorber growth for a same-substrate/Sb_2Se_3 interface. **Figure 1**a shows an SEM cross-section image of a device where Sb_2Se_3 films were grown on sp-TiO_2 under the growth conditions optimized for sol-TiO_2. Significant interfacial voiding and possible delamination is observed, as seen elsewhere in Sb_2Se_3 literature incorporating TiO_2 as a partner layer.[45,75] The sol-TiO_2 deposited via liquid spin-casting fills depressions in the highly textured FTO (Figure 1b), producing a smooth surface on which to grow the Sb_2Se_3 films. However this results in natural variance in TiO_2 film thickness (50–120 nm). Due to the nature of the TiO_2 film deposition via the sputtered method, the sp-TiO_2 conformally coats the FTO (Figure 1a,c),

providing a window layer with a more uniform thickness across the substrate (60–80 nm), but also a surface roughness equal to that of the underlying substrate which has implications for Sb_2Se_3 film growth. Root mean square (RMS) roughness was subsequently determined for sol-TiO_2 and sp-TiO_2 films from AFM as 3.84 nm and 23.26 nm, respectively (Figure S1, Supporting Information).

An increase in substrate temperature to 400 °C during the seed layer deposition appeared to remedy the interfacial voiding as evidenced by a visible darkening of the device when viewed through the glass side (Figure S2, Supporting Information). Good adhesion of Sb_2Se_3 grains grown on the rough substrate is confirmed

ADVANCED
SCIENCE NEWS

www.advancedsciencenews.com

ADVANCED
MATERIALS
INTERFACES
Open Access
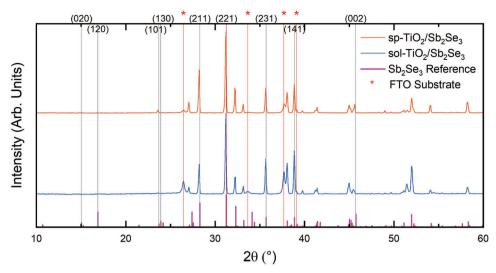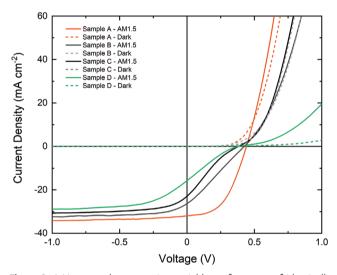
www.advmatinterfaces.de

Figure 2. θ-2θ X-ray diffraction patterns of Sb_2Se_3 films grown via CSS on both sol-TiO_2 and sp-TiO_2 window layers. Powder diffraction file (PDF) 9007437 for Sb_2Se_3 is included for reference. Miller indexing convention of the *Pbnm* setting of space group *62* is applied for Sb_2Se_3.[79]

by the cross-sectional TEM image in Figure 1c which shows no indication of void formation. The compact and uniform Sb_2Se_3 grain structure achieved on sol-TiO_2 via our two-step CSS process is maintained (Figure 1d,e), which is valuable in reducing the need for organic pinhole blocking layers (P3HT, Spiro-OMeTAD etc.) in superstrate device structures - although their inclusion is still required, at present, to reduce back contact barrier height and facilitate hole extraction.[57] At substrate temperatures in excess of 400 °C, increased grain size is observed and pinholes appear between grains as the seed layer is expended by agglomeration into larger grains (Figure S3, Supporting Information). In the case of the Sb_2Se_3 film grown on sol-TiO_2, we observe nanosized grain structures at the interface which are confirmed as antimony oxide via energy–dispersive X–ray spectroscopy (EDX) (Figure S4, Supporting Information). These crystallites have been observed previously in hydrothermally deposited Sb_2Se_3 films and were shown to be detrimental to device performance.[24] At this stage it is unclear if these antimony oxide regions are dependant on the interface layer or instead influenced by CSS deposition conditions.

Vast amounts of antimony chalcogenide literature focuses on optimising vertical growth orientation of 1D nanoribbons.[33,34] This is due to the supposed enhanced conductivity along the direction of the ribbons compared to inter-ribbon conductivity via traversal of van der Waal bonds which result from a stereochemically active lone pair orbital.[76–78] Despite a recent theoretical study which suggests this is an oversimplified view of the anisotropy in these materials,[29] (and record efficiencies with (hk0) oriented CBD devices[25,26]) it remains customary to eliminate ribbon growth parallel to the substrate. X-ray diffractograms for optimized Sb_2Se_3 films grown on both sol-TiO_2 and sp-TiO_2 are shown in **Figure 2**. Both films show no signal from (020), (120), and (130) planes characteristic of the (hk0) plane from ribbon growth parallel to the substrate.

This demonstrates that equally high quality films with good grain structure and vertical orientation can be produced on both sol-TiO_2 and sp-TiO_2. Despite the interface being nominally the

Figure 3. J–V curves demonstrating variable performance of identically fabricated Sb_2Se_3 devices with sp-TiO_2 window layers. Samples A–D correspond to each independent sputtering run under the same conditions.

same in both instances, that is, TiO_2/Sb_2Se_3, the change in surface roughness resulting from the two partner layer deposition methods strongly influences the growth of the Sb_2Se_3 absorber layer, as evidenced in Figure 1.

3.2. Interfacial Barriers

Upon fabricating devices using the sp-TiO_2 layer, a high degree of run to run variability was noticed. **Figure 3** shows J–V curves for contacts from four nominally identical devices, trivially named samples A–D, with independently sputtered TiO_2 layers and the associated performance parameters are given in **Table 1**. An obvious assumption would be that processing conditions and partner layer quality achieved for sol-TiO_2 are easily transferred,

**ADVANCED
SCIENCE NEWS**

www.advancedsciencenews.com

**ADVANCED
MATERIALS
INTERFACES**
Open Access

www.advmatinterfaces.de

Table 1. Device performance parameters extracted from the J–V curves of devices in Figure 3. Samples A–D correspond to each independent sputtering run under the same conditions.

Sample	PCE [%]	V_{oc} [V]	J_{sc} [mA cm^{-2}]	FF [%]
Sample A	6.88	0.44	31.98	48.77
Sample B	2.89	0.43	26.29	25.79
Sample C	1.81	0.38	22.92	20.65
Sample D	1.24	0.39	15.76	20.44

however huge performance variation was observed in the form of S-shaped distortion in current–voltage curves for some devices based on sp-TiO$_2$, which are widely diagnosed in PV literature as the existence of a barrier to charge extraction in the device.[80–83] The degree of S-shape was consistent in all subsequent devices fabricated from the same batch of sp-TiO$_2$ - that is, sputtering on four substrates simultaneously resulted in four devices (each with 16 contacts) with equivalent amount of S-shaped J–V distortion, irrespective of subsequent absorber and HTL processing. Thus it was determined that the J–V distortion is related to sp-TiO$_2$ film quality.

A number of sample series were made by changing the sputtering conditions (ambient oxygen content, film thickness, deposition temperature, chamber pressure, post-deposition annealing temperatures etc.), but the cause of the sp-TiO$_2$ run variability was not able to be identified. The extent as to which these interfacial barriers, formed by sp-TiO$_2$ layers, act to restrict device performance varies randomly but in extreme cases can reduce device performance from ≈7% to ≈1% PCE as a result of severe fill-factor loss.

Pjevic et al.[84] conducted an in-depth study of TiO$_2$ films, similarly sputtered from a compound target, although their post-deposition annealing was conducted in Ar atmosphere at 400 °C. It was found that a low anatase:rutile (A:R) ratio was obtained for high ambient O$_2$ flow during deposition, and the opposite for low O$_2$/Ar mass flow. For the sample sputtered without any O$_2$ ambient, no diffraction peaks associated with either anatase or rutile phases TiO$_2$ were obtained. Hsu et al.[85] reported that the presence of rutile microcrystals detected via Raman spectroscopy in as-deposited amorphous TiO$_2$, subsequently dictated the outcome of amorphous-crystalline transformation. This study compared ion-beam deposition techniques including reactive sputtering from a metallic Ti target.

S-shaped curves commonly arise in organic solar cells (OSC) where a variety of metal oxides like TiO$_2$ are employed as the partner layer. In OSC literature it is described as a 'light-soaking' issue whereby exposure to UV light can induce removal of the observed S-shape via realignment of band offsets at the junction interface. The same mechanism was not observed in these devices after isolating the UV component with high-pass optical filtered J–V measurement (Figure S5, Supporting Information).

To understand the source of the charge barriers, both the partner layer sp-TiO$_2$ films (post-annealing) and subsequent completed Sb$_2$Se$_3$ devices were characterized from the best (Sample A) and worst (Sample D) performing devices in Figure 3, along with a solution spin-cast TiO$_2$ film and resulting device which is much more typical of those found elsewhere in literature. For

simplification and readability, herein, reference films and devices are referred to and color-coded as follows; 'sol-TiO$_2$' (blue) for the established spin-cast solution TiO$_2$, 'peak sp-TiO$_2$' (orange) for the high performance sputtered TiO$_2$ film and 'barrier sp-TiO$_2$' (green) for the sputtered film which produced S-shaped J–V distortion in completed Sb$_2$Se$_3$ solar cell devices.

3.3. TiO$_2$ Bulk Characterization

To identify potential causes of the interfacial charge barriers present in sputtered TiO$_2$ devices, we compare the reference sol-TiO$_2$ and both peak and barrier sp-TiO$_2$ films with equivalent post-deposition annealing conditions of 500 °C for 30 min in air. Whilst the difficulties of characterising thin-films deposited on multi-layer transparent conducting oxide(TCO)-coated glass can be easily overcome by depositing thicker films on glass under the same conditions to simplify and enhance the signal of various characterization techniques, in many cases this is not a device relevant alternative due to drastically different substrate-dependant growth properties (particularly polymorphic materials), which ultimately dictate device performance.[86] Equally, the thin-films on FTO are required in this case to produce complete devices and determine the sp-TiO$_2$ film's eventual influence on J–V distortion. With this in mind, grazing incidence X-ray diffraction (GIXRD) was employed in an attempt to interrogate the structure of the ≈70 nm TiO$_2$ films (determined via SEM (Figure 1a,c)) deposited on FTO (**Figure 4**). Varying the incident angle revealed a strong signal from the underlying FTO substrate in all samples, with the sol-TiO$_2$ film (Figure 4a) showing obvious additional diffraction features at 25.4 ° and 48.0 ° attributed to anatase (101) and (200) lattice planes, respectively - which change in intensity relative to the FTO as the penetration depth is tuned by incident angle. These anatase features appear shifted to higher diffraction angle relative to the reference spectra and are broadened relative to the underlying FTO peaks, indicating that the the broadening is induced by small crystallite size. Any evidence of crystallinity in GIXRD of either the peak or barrier sp-TiO$_2$ films (Figure 4b,c) is limited only to a very weak peak near the anatase (101) diffraction angle. The differences between the spin-cast solution and sputtered films are unlikely to be due to thickness variations, and moreover diffraction from the sol-TiO$_2$ is very strong. Instead, this result indicates that poor crystallinity (or a lack of long-term order) may be present in devices fabricated via the room temperature sputtering method, despite it undergoing identical post-deposition annealing conditions as the sol-TiO$_2$ film. Both the peak and barrier sp-TiO$_2$ samples however, show a similar lack of crystallinity, making it possible that crystallinity alone is not the principal cause of J–V shape differences.

As an alternative method of bulk phase identification, Raman spectroscopy was used for TiO$_2$ characterization on the same set of samples. Spectral Raman mapping for a grid of 10x10 points with a 10 μm increment over a 100 μm^2 total area was each conducted for sol-TiO$_2$, peak sp-TiO$_2$, and barrier sp-TiO$_2$. This allows for spatial representation of phase arrangement due to the smaller associated spot size in Raman compared to GIXRD and beamline soft XPS shown later. Acquired spectra from all 100 points for each sample are plotted in **Figure 5**a–c after background subtraction of bare FTO spectra and the positions of
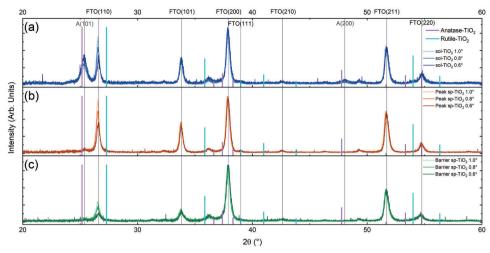
Figure 4. GIXRD of a) sol-TiO$_2$, b) peak sp-TiO$_2$, and c) barrier sp-TiO$_2$ films grown on FTO, with varying incident angle. Data has been normalized to the FTO(200) peak. Also included are PDF cards 9008216 (purple) and 9004143 (cyan) with peak positions for a-TiO$_2$ and r-TiO$_2$, respectively.

anatase (purple) and rutile (cyan) vibrational modes taken from the literature are included for reference.[52,87] For the sol-TiO$_2$, peaks are observed at 145, 398, 515, and 635 cm^{-1}, consistent with anatase phase confirming the result from sol-TiO$_2$ GIXRD diffractograms in Figure 4a. In both the peak and barrier sp-TiO$_2$ films (Figure 5b,c), peaks consistent with literature for vibrational modes of rutile are seen at 444 and 610 cm^{-1}, which are clearly absent in the sol-TiO$_2$ sample. These broad low intensity rutile peaks, particularly in the peak sp-TiO$_2$ film, are further evidence of poor crystallinity in these films and can be found enhanced in Figure S6 (Supporting Information) before background subtraction and signal scaling. Hence whereas there is no evidence of *crystalline* r-TiO$_2$ in GIXRD of the sputtered films, the Raman result indicates its presence in disordered form. If present, it would inhibit widespread formation of the less-stable anatase phase in sputtered films.

Interestingly, spectra obtained from the barrier sp-TiO$_2$ film, which produced S-shaped distortion in the J–V curves of completed Sb$_2$Se$_3$ devices, also demonstrates spatially inhomogeneous anatase character, by the presence of varying intensity from the 145 cm^{-1} anatase vibrational mode in addition to the consistent rutile signal. The point-to-point anatase intensity variance highlighted in Figure 5d is plotted as a function of XY position in Figure 5e, normalized to the most intense 145 cm^{-1} peak co-ordinate (purple).

It should be noted that an in-depth study by J. Zhang et al.[87] observed that their Raman spectra was dominated by the anatase 143 cm^{-1} mode, even in cases where A:R=1:15, and so the relative intensities are not necessarily indicative of A:R phase weighting. This would imply that the anatase content in the random distribution of mixed-phase pockets in the barrier sp-TiO$_2$ film may be small, despite significant signal intensity relative to rutile. This same study also found that at $\leqslant$ 500 °C calcination temperatures, 0% rutile content was observed via either XRD or Raman methods, but found that during the anatase/rutile phase transition, anatase can remain at the surface at higher temperatures compared to the bulk. S. Zhang et al.[86] suggested that the rutile crystal structure of SnO$_2$:F acted as a template to encourage

the formation of r-TiO$_2$ at the FTO/TiO$_2$ interface, however this explanation fails to explain the lack of rutile signal present in sol-TiO$_2$ films also deposited on FTO.

Given the contrast in crystallinity obtained for sol-TiO$_2$ and peak sp-TiO$_2$ films, which both delivered impressive Sb$_2$Se$_3$ device performance, it is unlikely that this is the origin of the charge barrier which varies in influence from deposition to deposition. The presence of rutile in the peak sp-TiO$_2$ film also suggests that the rutile phase alone is not inherently unfavorable for a TiO$_2$/Sb$_2$Se$_3$ junction, although single phase samples from both methods would be required for a more direct comparison. A much more likely scenario is that, the density of anatase grain formation within the surrounding rutile material varies across sputtering runs and is somehow the source of the varying size of this barrier to charge extraction. From this bulk measurement alone, it cannot be identified whether the anatase present in the multi-phase barrier sp-TiO$_2$ film is constrained to the TiO$_2$ film surface, or buried below.

We anticipate that the higher energy deposition of the sputtered method here and resulting disorder from the same amorphous rutile microcrystal mechanism observed by Hsu et al.[85] induces a high partner layer defect density, shown by the same group to induce J–V distortion in CdS/CI(G)S devices.[88]

3.4. TiO$_2$ Surface Characterization

Whilst the GIXRD and Raman results allow assessment of the bulk phase character of TiO$_2$ layers, it is necessary to independently investigate the film surface which interfaces the absorber in the heterojunction device. The electron inelastic mean free path, which results in an exponential signal intensity decay in X-ray photoemission spectroscopy (XPS), provides a probing depth of just the top $\approx$5 nm for soft X-ray photon energies like those used here. This allows for an isolated measurement of the TiO$_2$ surface. Valence band (VB) XPS has been employed previously for phase quantification of mixed phase TiO$_2$ powders, due to the distinct difference in VB spectral shape of anatase and rutile.[89]

ADVANCED
SCIENCE NEWS
www.advancedsciencenews.com

ADVANCED
MATERIALS
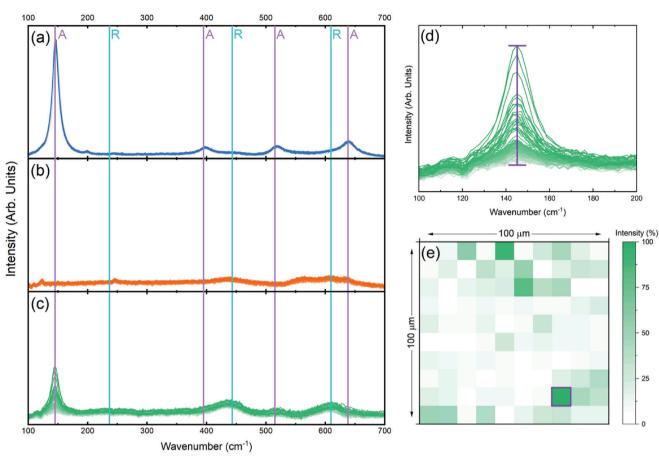**INTERFACES**
Open Access
www.advmatinterfaces.de

Figure 5. Raman spectra of reference a) sol-TiO$_2$, b) peak sp-TiO$_2$, and c) barrier sp-TiO$_2$ films grown on FTO. d) Barrier sp-TiO$_2$ anatase peak intensity. e) Raman mapping of barrier sp-TiO$_2$ 145 cm^{-1} peak intensity. λ_{ex} = 532 nm.

Figure 6 shows experimental VB XPS spectra from the reference sol-TiO$_2$, peak sp-TiO$_2$ and barrier sp-TiO$_2$ films, overlayed with VB partial (pDoS) and total electronic density of states (tDoS) calculated from density functional theory (DFT) for the two relevant polymorphs. The binding energy (BE) scale is set here to align with unbroadened theoretical tDoS which aligns the valence band maximum (VBM) at 0 eV. The experimental data is shifted to match spectral features which allows for phase identification. Details of the applied photoionization cross-section correction and simulated broadening effects for the DFT are included in Figures S7 and S8 (Supporting Information).

Significant differences in spectral shape is observed dependant on the film deposition method with a stronger low BE feature in both the peak and barrier sp-TiO$_2$, whilst the highest intensity VB feature in sol-TiO$_2$ arises deep into the VB at ≈4 eV. The sol-TiO$_2$ and sp-TiO$_2$ spectra are identified as anatase and rutile, respectively, due to the strong agreement observed between experiment and the predicted tDoS from DFT, along with single crystal and powder references (albeit at slightly higher photon energy) (Figure S9, Supporting Information).

The pDoS in both polymorphs predicts significant contribution to the spectra from Ti p orbitals, and the experimental agreement confirms that this is the primary influence on VB spectral shape at these photon energies. Whilst the relative contribution of Ti p states to the overall spectra is comparable between anatase

and rutile, the overall shape differs due to chemical bonding and orbital hybridization which evidently distinguishes the polymorphism of TiO$_2$. We note that TiO$_2$ oxidation states and thus valency occupation is not fully understood,[90] with semi-core Ti 3p predicted to display valency character in some cases,[91,92] whilst other studies predict[93] and evidence[94,95] Ti 4p occupation - which would require estimation of the corresponding photoionization cross-section which is not included in either Scofield[96] or Yeh and Lindau[97] calculations. This may of course be phase dependant as discussed by Thomas et al.[95] who found from resonant photoemission that Ti 4sp hybridization was present in the rutile phase only. For TiO$_2$ phase identification, we have simplified this by assuming Ti 3p valency is sufficient for this purpose. However, it is acknowledged that assuming complete 3p or 4p valency orbital occupation is insufficient in recreating experimental spectra at both soft and hard X-ray energies concurrently, which would perhaps allow for bulk phase identification via this method.[98,99]

Based on the work by Breeson et al.,[89] even a 1:10 A:R film would alter the spectra to produce equal intensity from both low and high BE VB features (assuming depth homogeneity). Whilst the single-phase surface results observed here are expected for the samples which demonstrated single-phase character in the respective Raman spectra; when we apply this to the film which exhibited multi-phase vibrational modes, that is, the
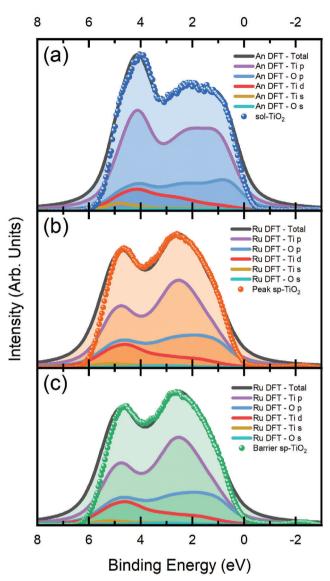
Figure 6. XPS valence band data for a) sol-TiO$_2$ at $h\nu$ = 1090 eV and b) peak sp-TiO$_2$ and c) barrier sp-TiO$_2$ at $h\nu$ = 800 eV with a shirley background subtraction. Experimental data is overlayed with theoretical DFT calculations for (a) anatase and (b,c) rutile phase TiO$_2$.

barrier sp-TiO$_2$ film, we find that the surface shows no indication of an anatase component in the phase composition. This would indicate that the anatase phase identified in the Raman is buried below a rutile surface which will complicate charge transfer and band alignment at both sides of our TiO$_2$ interface in the FTO/TiO$_2$/Sb$_2$Se$_3$ system, which have previously been applied for single-phase TiO$_2$.[54,59,100]

3.5. Band Alignment

Figure 7a–c illustrates the phase architecture determined via the Raman and VB XPS in the respective reference TiO$_2$ films and their orientation with regard to subsequent Sb$_2$Se$_3$ deposition. From the bulk and surface phase analysis, we have identified

pure anatase in the sol-TiO$_2$ film and pure rutile in the peak sp-TiO$_2$ film. Whilst the Raman results in Figure 5e clearly demonstrate an inhomogenous a-TiO$_2$ distribution in the barrier sp-TiO$_2$ film, for the purpose of band alignments, it is assumed that the density of sub-surface anatase is correlated with J–V distortion and thus the barrier sp-TiO$_2$ device stack is approached as an FTO/a-TiO$_2$/r-TiO$_2$/Sb$_2$Se$_3$ structure. This further complication of charge transfer and band alignment at the anatase/rutile interface has been studied for photocatalytic applications,[71,101–103] but also in the case of PV application as a 'phase junction'.[104–107] The evidence presented by Scanlon et al.[71] and Pfeifer et al.[101] supports a type-II anatase band alignment encouraging electron(hole) flow from(to) rutile to(from) anatase, although alternative interpretations have been explored.[103]

Band alignment measurements are regularly incorporated into studies of heterojunction PV devices, particularly whenever the material environment at a near-interface (typically window/absorber) is varied. The most common method is a 'natural' band alignment which requires precise measurement of a materials VBM (relative to the fermi level (E_F)) and secondary electron cutoff (SEC), which together provide a value of the ionization potential (IP) relative to vacuum level. Once the value of the IP is known, band gaps are applied to find the conduction band minima (CBM) position. Natural band alignments alone are somewhat limited, as they do not account for charge transfer, alignment of fermi levels and resultant band bending upon contact of material interface. This is highlighted by the contrast in conduction band offsets (CBO) at the a-TiO$_2$/Sb$_2$Se$_3$ interface measured by Shiel et al.[59] when applying various band alignment techniques. We propose a more suitable application of the natural band alignment process is to look at relative changes in band position for different samples of the same material. For efficient electron extraction across both the absorber/window and window/TCO interfaces, the CBM position is critical - which first requires reliable TiO$_2$ band gap determination.

In cases where optical analysis is used to determine film band gaps, it is not uncommon to simplify analysis by measurement of films deposited on glass, rather than TCO-coated substrates. Another method is to avoid direct measurement entirely by adopting theoretical or literature reported band gaps, which often assume bulk samples in contrast to the ultra thin (<100 nm) films relevant for device application. Whilst this is valid in some cases, deposition conditions (including growth substrate) clearly impact material properties in a significant way.[86] Assumptions made in optical band gap measurements have particular causal implications when incorporated into band alignment measurements, which is perhaps one reason why reported CBOs between TiO$_2$/Sb$_2$Se$_3$ vary so widely.[53,54,59,100]

Specifically, interpretation of TiO$_2$ is complicated by the polymorphs with rutile and anatase having similar indirect band gap values of 3.0 and 3.2 eV, respectively.[71] Rutile is reported to be a direct band gap semiconductor, however the transition is parity forbidden, which should result in extremely weak absorption. Whilst this has implications for band gap measurement via optical transition, in the case of applications in PV as an electron transport layer, we are mainly interested in the minimum energy state of the conduction band for alignment with the absorber material for efficient carrier extraction. This may not necessarily be measurable - by optical measurement for forbidden transitions,

**ADVANCED
SCIENCE NEWS**
www.advancedsciencenews.com

**ADVANCED
MATERIALS
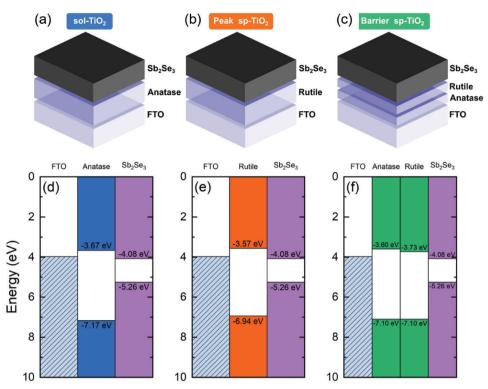INTERFACES**
Open Access
www.advmatinterfaces.de

Figure 7. Illustration of reference device stacks for a) sol-TiO$_2$, b) peak sp-TiO$_2$ and c) barrier sp-TiO$_2$. Band positions extracted from VB and SEC XPS measurements for (a) sol-TiO$_2$, (b) peak sp-TiO$_2$, and (c) barrier sp-TiO$_2$. sol-TiO$_2$, and Sb$_2$Se$_3$ data recreated with permission from Shiel et al.[59]

but also in the case of degenerately doped materials (not uncommon for metal oxides) where the lowest conduction states are occupied, resulting in Burstein-Moss shifts of band gap values extracted via the Tauc approach. This effect is particularly apparent in TCOs where the electronic band gap and optical band gaps are reported independently,[60] but may also be necessary here due to the large VBM positions relative to E_F measured which almost meet the reported bulk band gaps of rutile and anatase for sp-TiO$_2$ (2.98 eV) and sol-TiO$_2$ (3.14 eV), respectively (Figure S10a,b, Supporting Information).

Nevertheless, we report indirect optical band gaps measured by the initial linear onset of the Tauc plot from UV–vis transmission and reflection measurements for the anatase sol-TiO$_2$ and rutile peak sp-TiO$_2$ as 3.50 eV and 3.37 eV, respectively (Figure S11, Supporting Information). No linear fit could be confidently applied to the spectra from our mixed phase barrier sp-TiO$_2$ film to provide a reliable band gap value, partially due to interference fringes caused by the thin-films, and partly due to the multi-phase nature of the film grown on top of the FTO which will certainly contribute to a staggered absorption onset. For the purpose of band alignment determinations of the barrier sp-TiO$_2$ sample, the rutile band gap was used for the r-TiO$_2$/Sb$_2$Se$_3$ interface while the anatase band gap was used for the a-TiO$_2$/FTO interface. VBM and SEC positions were measured via lab XPS for FTO and the reference films to determine the IP (Figure S10, Supporting Information).

Comparing first the band positions of the pure anatase phase sol-TiO$_2$ (Figure 7d) and pure rutile phase peak sp-TiO$_2$ (Figure 7e), we report a considerably lower IP in the sol-TiO$_2$

film than the peak sp-TiO$_2$, which somewhat offsets the difference in CBM due to the larger band gap such that the peak sp-TiO$_2$ lies 0.10 eV higher relative to sol-TiO$_2$. This results in a CBO between TiO$_2$/Sb$_2$Se$_3$ of 0.51 and 0.41 eV for the peak sp-TiO$_2$ and sol-TiO$_2$, respectively. Whilst this measured offset would be considered large enough to induce a charge extraction barrier, as we have seen, natural band alignments alone are not conclusive. Thus, looking at the relative change in TiO$_2$ band position for the reference samples in this study, the IP measured from the barrier sp-TiO$_2$ film lies between that of the anatase sol-TiO$_2$ and rutile peak sp-TiO$_2$ film, which seems reasonable for a film comprising the two polymorphs. Applying the band alignment in Figure 7f such that the device is structured as FTO/a-TiO$_2$/r-TiO$_2$/Sb$_2$Se$_3$ returns CBM positions unremarkably different from the films which produced high FF photovoltaic devices. In fact, the the staggered band gaps provide a smaller CBO at each interface which would be expected to enhance carrier extraction. We therefore surmise that the anatase/rutile interface to be the source of the charge extraction barrier in this case, rather than a CBO issue which appears to be the focus of much research.

3.6. Device Characterization

Despite the issues with phase control and crystallinity in the sp-TiO$_2$ window layers, it was observed that they produced higher values of both J_{sc} and V_{oc} in the peak devices. To highlight the influence of the TiO$_2$ window layer deposition method on FTO/TiO$_2$/Sb$_2$Se$_3$/P3HT/Au device performance, the
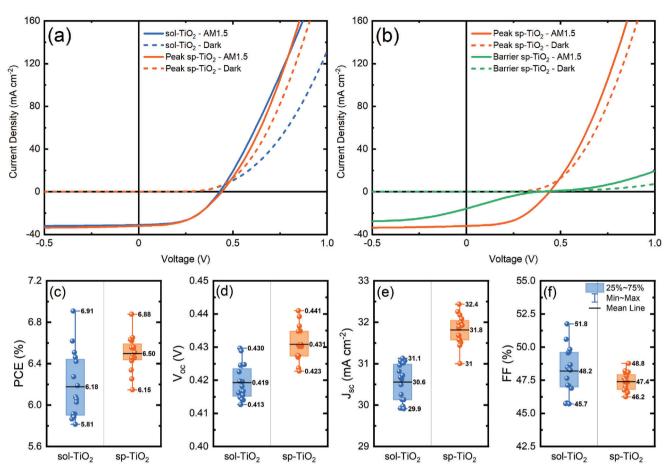
Figure 8. a) Current density-voltage measurements comparing peak performance devices from sol-TiO$_2$ and sp-TiO$_2$. b) Comparison of J–V curves from peak and barrier sp-TiO$_2$ devices. c–f) Box and whisker plots for parameters extracted from J–V measurement for peak devices fabricated via both methods (*n* = 16).

highest performing devices fabricated with spin-cast solution (sol-TiO$_2$) and sputtered window layers (sp-TiO$_2$) are compared in **Figure 8**a. These devices are prepared as discussed in Section '2.1 Device Fabrication', with the re-optimized CSS conditions employed for the sp-TiO$_2$ device to grow Sb$_2$Se$_3$ effectively, as discussed in Section '3.1 CSS Re-optimization for sp-TiO$_2$'. Sample D from Figure 3 is shown again here (Figure 8b) for reference and used for subsequent EQE measurement.

Comparing the J–V curve from champion performance sol-TiO$_2$ and sp-TiO$_2$ contacts (Figure 8a), it is observed that the sp-TiO$_2$ demonstrates an improvement in both J_{sc} and V_{oc}. However the *PCE* is comparable due to a reduced *FF*, which is linked to the non-linearity present in the forward bias regime. 'Crossover' is present in both samples, where the illuminated J–V curve crosses the dark J–V near V_{oc}. This is associated with interfacial barriers caused by conduction band offsets and photoinduced changes of trap occupancy in the partner layer.[108,109]

The extracted J–V parameters of 16 contacts across each device are shown in Figure 8c–f. Whilst the *PCE* of the highest performing sol-TiO$_2$ contact (blue) slightly outperforms that of the sp-TiO$_2$ (orange), performance uniformity across the substrate is much improved in the sp-TiO$_2$, demonstrated by the tighter *PCE* spread and notable increase in mean *PCE* from 6.18% for sol-

TiO$_2$ to 6.50% in the sp-TiO$_2$ (Figure 8c). We attribute the device uniformity improvement to the conformal sputtered deposition of the TiO$_2$ film which provides a consistent film thickness in contrast to the solution spin-cast film which is observed to have varying film thickness over the rough FTO surface (Figure 1b,c). This solution process is also prone to variation in deposition quality due to surface contamination and uneven distribution of the spun solution. Although not directly observed in the cross-sectional SEM images, areas of extreme FTO roughness or uneven coverage could result in islands protruding through sol-TiO$_2$, resulting in direct FTO/Sb$_2$Se$_3$ contact, which would certainly reduce device performance due to inconsistency in junction quality and weak diode regions.[110]

Figure 9 shows EQE data for the three reference devices together with the cumulative integrated J_{sc}. The band gap positions for Sb$_2$Se$_3$ and the appropriate phases of TiO$_2$ are marked for reference.[6]

The most striking difference observed in dark EQE spectra of the reference devices is the much increased long wavelength collection in the peak sp-TiO$_2$ pure rutile film (relative to anatase sol-TiO$_2$) which provides a clean 'top hat' shape and a high integrated J_{sc} well in excess of 30 mA cm^{-2} (Figure 9a,b) (grey), consistent with the improved reverse bias saturation current
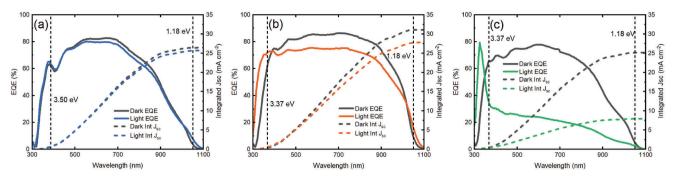
ADVANCED
SCIENCE NEWS
www.advancedsciencenews.com

ADVANCED
MATERIALS
INTERFACES
Open Access
www.advmatinterfaces.de

Figure 9. Both dark and light-biased EQE measurements and calculated J_{sc} from EQE for a) sol-TiO$_2$, b) peak sp-TiO$_2$, and c) barrier sp-TiO$_2$.
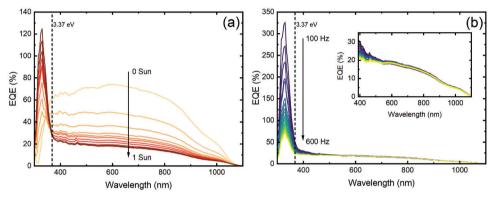

Figure 10. a) EQE spectra for barrier sp-TiO$_2$ device under varying light bias at 295 Hz chopping frequency. b) EQE spectra for barrier sp-TiO$_2$ device under 1 sun illumination with a varied chopping frequency.

under illumination in the J–V curves of high performing sp-TiO$_2$ devices. This enhanced long wavelength collection is not maintained in the multi-phase barrier sp-TiO$_2$ device (Figure 9c). However, the integrated J_{sc} measured from EQE remains comparable to established sol-TiO$_2$, which is obviously not recreated in the illuminated J–V curve in Figure 8b (green line) which demonstrates S-shaped characteristics. We also observe that the peak of the short wavelength onset shifts toward longer wavelength in the pure rutile film Figure 9b, relative to the higher band gap anatase containing films (Figure 9a,c) due to window layer absorption of photons with energy in excess of the optical band gap which will recombine as a result of absorption outside of the depletion region.

Due to the obvious discrepancy between the extracted integrated J_{sc} from dark EQE and J–V measurement under AM1.5G illumination in the barrier sp-TiO$_2$ devices, additional EQE spectra were obtained under white light-biasing of the sample. For the highly anatase sol-TiO$_2$ device, which demonstrates no S-shaped J–V characteristic, there is a minor change in quantum efficiency between the standard EQE measurement and the light-biased EQE (Figure 9a). For both sp-TiO$_2$ films however, significant transformation of the spectra is observed (Figure 9b,c). The device fabricated from the multi-phase film which demonstrated S-shape behavior in J–V curves shows a collapse in quantum efficiency in the typical operational wavelength range (Figure 8c). The proposed barrier limiting charge extraction is thus clearly induced by device illumination. This effect of reduced EQE is also present in the peak sp-TiO$_2$ device, which explains the reduced

FF in peak sp-TiO$_2$ devices compared with sol-TiO$_2$, limiting the device PCE despite demonstrating improved V_{oc} and J_{sc}. It seems reasonable to assume that these sputtered TiO$_2$ window layers are capable of achieving record J_{sc}, provided the observed illumination losses can be eradicated. Another interesting feature in the light-biased EQE spectra is the short wavelength onset which shifts significantly in to the UV range for photons above the window layer band gap energy.

To further investigate the increase in blue light collection in sp-TiO$_2$ partner layer devices under illumination, additional spectra were obtained with a varied light-bias for the barrier sp-TiO$_2$ device (**Figure 10**a). Whilst the sub-TiO$_2$-band gap collection reduced with increasing intensity of applied light-bias, the opposite was observed for wavelengths with energy in excess of the TiO$_2$ band gap. This effect continued to increase blue-light collection past 0.8 sun illumination where the EQE yield surpasses unity at 330 nm, which of course must be caused by an abnormality in the measurement. EQE exceeding 100% in the UV range has previously been reported in defective and photoconductive TiO$_2$.[111] A similar mechanism is seen in CdS/CdTe and CdS/Chalcogenide devices whereby the photoconductive CdS window layer conductivity is modulated with the frequency of the AC chopped monochromated probing beam in the blue region.[112–114] The increased CdS conductivity widens the depletion region further into the absorber, increasing red light generated carriers under light-bias which are collected in-phase with the chopped blue probing beam due to the conductivity modulation. The work by Hegedus[112] and Liu et al.[114] showed that this effect can be

**ADVANCED
SCIENCE NEWS**

www.advancedsciencenews.com

**ADVANCED
MATERIALS
INTERFACES**
Open Access

www.advmatinterfaces.de

manipulated by altering the chopping frequency due to the slow CdS trap response time. Figure 10b demonstrates the dependence of chopping frequency on EQE measurement of the barrier sp-TiO$_2$ device, which shows characteristics similar to that seen in CdS, although constrained to a narrower wavelength range due to the wider TiO$_2$ band gap. This is also present to a lesser extent in the peak sp-TiO$_2$ device, but absent in sol-TiO$_2$ (Figure S12, Supporting Information).

The light-biased EQE results indicate increased photoconductivity in TiO$_2$ films obtained via the sputtered deposition method. Whilst the effects of photoconductivity on 'apparent' quantum efficiency are obvious in Figure 10b, the long wavelength collection shows no dependence on chopping frequency (Figure 10b, inset). It is therefore not clear that the photoconductivity is directly responsible for the formation of interfacial charge barriers in these devices. Although the photoconductivity itself may not be the source of J–V distortion, a high defect density in the sp-TiO$_2$ films might be. Future work will focus on understanding the sputtered TiO$_2$ photoconductivity and determining whether this is linked to the density of mixed-phase anatase/rutile films, and thus the formation of interfacial charge barriers under illumination limiting the FF in these Sb$_2$Se$_3$ devices.

4. Conclusion

In this study, we have demonstrated that high quality Sb$_2$Se$_3$ films can be grown via CSS on highly scalable RF magnetron sputtered TiO$_2$ window layers, which conformally coat the rough surface of the underlying FTO. The highest performing devices fabricated from sp-TiO$_2$ films deliver improved J_{sc} and V_{oc} values of 32.44 mA cm^{-2} and 441 mV respectively, compared with spin-cast solution TiO$_2$ films. Issues with reproducibility in sp-TiO$_2$ films is observed whereby varying S-shape J–V distortion is present in completed Sb$_2$Se$_3$ devices, which indicates the presence of interfacial barriers limiting charge extraction. We demonstrate suitable methods for separating surface and bulk TiO$_2$ phase character, through matching experimental and theoretical VB spectral features in surface sensitive XPS and deeper penetrating Raman spectroscopy and GIXRD.

Thorough characterization of three TiO$_2$ partner layer films and resulting devices are compared to identify the source of these charge barriers, which vary between sputtering runs. This comparison comprised both a high (peak sp-TiO$_2$) and low (barrier sp-TiO$_2$) performance sputtered film, and a highly reproducible spin-cast solution (sol-TiO$_2$) film. Through the aforementioned characterization methods, we identify pure anatase phase in the sol-TiO$_2$ film and pure rutile phase in the peak sp-TiO$_2$ film. Whilst the barrier sp-TiO$_2$ film demonstrated a pure rutile surface layer via XPS, an inhomogeneous distribution of anatase was discovered in the bulk via Raman mapping of a 100 μm^2 area. Relative band positions of these films show no obvious reason for S-shape formation caused by a CBO. The observed charge barriers are therefore likely due to interface interactions between phases. GIXRD diffractograms of both sp-TiO$_2$ films showed no diffraction signal of the rutile phase identified via Raman which indicates the films obtained via sputtering are highly disordered, despite undergoing identical post-deposition annealing as the highly crystalline anatase sol-TiO$_2$. We find that pure rutile phase

TiO$_2$ partner layers are capable of producing Sb$_2$Se$_3$ devices of equally high quality as the widely incorporated anatase phase.

Light-biased EQE measurement of completed Sb$_2$Se$_3$ devices exposes the presence of the interfacial charge barriers, which remain present to some extent in the peak sp-TiO$_2$ device. High photoconductivity in sp-TiO$_2$ films is identified due to EQE exceeding unity in the blue region under white light-bias, which is further evidence that the sputtering method produces highly defective TiO$_2$ films which introduce the S-shape J–V distortion.

The work presented here shows that TiO$_2$ phase control is reliant on more factors than simply sintering temperature, which is significant considering TiO$_2$ phase is not always confirmed in Sb$_2$Se$_3$ device literature. This is perhaps one of the reasons comparatively few groups are reporting high efficiency TiO$_2$/Sb$_2$Se$_3$ heterojunction devices, despite the clear limitations of CdS/Sb$_2$Se$_3$ structures. This result has implications for groups attempting to transition either from CdS partner layers to TiO$_2$, or even for transition from one TiO$_2$ deposition method to another. Further, these findings will also have relevance for other photovoltaic technologies such as perovskites and organic solar cells which more commonly utilize TiO$_2$ partner layers. Future work will focus on determining whether the distribution of mixed anatase and rutile phases in the films introduce photoconductive defects which are responsible for the observed interfacial charge barriers.

Conflict of Interest

The authors declare no conflict of interest.

Data Availability Statement

The data that support the findings of this study are openly available in Zenodo at https://doi.org/10.5281/zenodo.7752539.

ADVANCED
SCIENCE NEWS

www.advancedsciencenews.com

ADVANCED
MATERIALS
INTERFACES

www.advmatinterfaces.de

[1] S. Chen, Y. Fu, M. Ishaq, C. Li, D. Ren, Z. Su, X. Qiao, P. Fan, G. Liang, J. Tang, *InfoMat* **2023**, *5*, e12400.

[2] S. Chen, T. Liu, Z. Zheng, M. Ishaq, G. Liang, P. Fan, T. Chen, J. Tang, *J. Energy Chem.* **2022**, *67*, 508.

[3] W. Yang, J. H. Kim, O. S. Hutter, L. J. Phillips, J. Tan, J. Park, H. Lee, J. D. Major, J. S. Lee, J. Moon, *Nat. Commun.* **2020**, *11*, 861.

[4] W. Yang, J. Park, H.-C. Kwon, O. S. Hutter, L. J. Phillips, J. Tan, H. Lee, J. Lee, S. D. Tilley, J. D. Major, J. Moon, *Energy Environ. Sci.* **2020**, *13*, 4362.

[5] D. A. Garcia-Osorio, T. P. Shalvey, L. Banerji, K. Saeed, G. Neri, L. J. Phillips, O. S. Hutter, C. Casadevall, D. Antón-García, E. Reisner, J. D. Major, A. J. Cowan, *Chem. Commun.* **2023**, *59*, 944.

[6] M. Birkett, W. M. Linhart, J. Stoner, L. J. Phillips, K. Durose, J. Alaria, J. D. Major, R. Kudrawiec, T. D. Veal, *APL Mater.* **2018**, *6*, 084901.

[7] H. El-Shair, A. Ibrahim, E. Abd El-Wahabb, M. Afify, F. Abd El-Salam, *Vacuum* **1991**, *42*, 911.

[8] S. Messina, M. T. Nair, P. K. Nair, *J. Electrochem. Soc.* **2009**, *156*, H327.

[9] Y. Zhou, M. Leng, Z. Xia, J. Zhong, X. Liu, B. Yang, J. Zhang, J. Chen, K. Zhou, J. Han, Y. Cheng, J. Tang, *Adv. Energy Mater.* **2014**, *4*, 1301846.

[10] X. Wang, R. Tang, C. Wu, C. Zhu, T. Chen, *J. Energy Chem.* **2018**, *27*, 713.

[11] R. Tang, Z.-H. Zheng, Z.-H. Su, X.-J. Li, Y.-D. Wei, X.-H. Zhang, Y.-Q. Fu, J.-T. Luo, P. Fan, G.-X. Liang, *Nano Energy* **2019**, *64*, 103929.

[12] N. Fleck, O. S. Hutter, L. J. Phillips, H. Shiel, T. D. C. Hobson, V. R. Dhanak, T. D. Veal, F. Jückel, K. Durose, J. D. Major, *ACS Appl. Mater. Interfaces* **2020**, *12*, 52595.

[13] Z. Li, X. Liang, G. Li, H. Liu, H. Zhang, J. Guo, J. Chen, K. Shen, X. San, W. Yu, R. E. Schropp, Y. Mai, *Nat. Commun.* **2019**, *10*, 1.

[14] T. Liu, X. Liang, Y. Liu, X. Li, S. Wang, Y. Mai, Z. Li, *Adv. Sci.* **2021**, *8*, 2100868.

[15] Z. Duan, X. Liang, Y. Feng, H. Ma, B. Liang, Y. Wang, S. Luo, S. Wang, R. E. I. Schropp, Y. Mai, Z. Li, *Adv. Mater.* **2022**, *34*, 2202969.

[16] R. Tang, S. Chen, Z.-H. Zheng, Z.-H. Su, J.-T. Luo, P. Fan, X.-H. Zhang, J. Tang, G.-X. Liang, *Advanced Materials* **2022**, *34*, 2109078.

[17] Y. Luo, G. Chen, S. Chen, N. Ahmad, M. Azam, Z. Zheng, Z. Su, M. Cathelinaud, H. Ma, Z. Chen, P. Fan, X. Zhang, G. Liang, *Adv. Funct. Mater.* **2023**, *33*, 2213941.

[18] X. Wen, C. Chen, S. Lu, K. Li, R. Kondrotas, Y. Zhao, W. Chen, L. Gao, C. Wang, J. Zhang, G. Niu, J. Tang, *Nat. Commun.* **2018**, *9*, 2179.

[19] J. Tao, X. Hu, Y. Guo, J. Hong, K. Li, J. Jiang, S. Chen, C. Jing, F. Yue, P. Yang, C. Zhang, Z. Wu, J. Tang, J. Chu, *Nano Energy* **2019**, *60*, 802.

[20] T. D. C. Hobson, L. J. Phillips, O. S. Hutter, H. Shiel, J. E. N. Swallow, C. N. Savory, P. K. Nayak, S. Mariotti, B. Das, L. Bowen, L. A. H. Jones, T. J. Featherstone, M. J. Smiles, M. A. Farnworth, G. Zoppi, P. K. Thakur, T.-L. Lee, H. J. Snaith, C. Leighton, D. O. Scanlon, V. R. Dhanak, K. Durose, T. D. Veal, J. D. Major, *Chem. Mater.* **2020**, *32*, 2621.

[21] R. Tang, X. Wang, W. Lian, J. Huang, Q. Wei, M. Huang, Y. Yin, C. Jiang, S. Yang, G. Xing, S. Chen, C. Zhu, X. Hao, M. A. Green, T. Chen, *Nat. Energy* **2020**, *5*, 587.

[22] K. Shen, Y. Zhang, X. Wang, C. Ou, F. Guo, H. Zhu, C. Liu, Y. Gao, R. E. I. Schropp, Z. Li, X. Liu, Y. Mai, *Adv. Sci.* **2020**, *7*, 2001013.

[23] K. Li, Y. Lu, X. Ke, S. Li, S. Lu, C. Wang, S. Wang, C. Chen, J. Tang, *Solar RRL* **2020**, *4*, 2000220.

[24] D. Liu, R. Tang, Y. Ma, C. Jiang, W. Lian, G. Li, W. Han, C. Zhu, T. Chen, *ACS Appl. Mater. Interfaces* **2021**, *13*, 18856.

[25] Y. Zhao, S. Wang, C. Li, B. Che, X. Chen, H. Chen, R. Tang, X. Wang, G. Chen, T. Wang, J. Gong, T. Chen, X. Xiao, J. Li, *Energy Environ. Sci.* **2022**, *15*, 5415.

[26] Y. Zhao, S. Wang, C. Jiang, C. Li, P. Xiao, R. Tang, J. Gong, G. Chen, T. Chen, J. Li, X. Xiao, *Adv. Energy Mater.* **2022**, *12*, 2103015.

[27] J. Britt, C. Ferekides, *Appl. Phys. Lett.* **1993**, *62*, 2851.

[28] J. D. Major, R. E. Treharne, L. J. Phillips, K. Durose, *Nature* **2014**, *511*, 334.

[29] X. Wang, Z. Li, S. R. Kavanagh, A. M. Ganose, A. Walsh, *Phys. Chem. Chem. Phys.* **2022**, *24*, 7195.

[30] C. Jiang, J. Zhou, R. Tang, W. Lian, X. Wang, X. Lei, H. Zeng, C. Zhu, W. Tang, T. Chen, *Energy Environ. Sci.* **2021**, *14*, 359.

[31] K. Li, C. Chen, S. Lu, C. Wang, S. Wang, Y. Lu, J. Tang, *Adv. Mater.* **2019**, *31*, 1903914.

[32] F. Pattini, S. Rampino, F. Mezzadri, D. Calestani, G. Spaggiari, M. Sidoli, D. Delmonte, A. Sala, E. Gilioli, M. Mazzer, *Sol. Energy Mater. Sol. Cells* **2020**, *218*, 110724.

[33] S. Chen, T. Liu, M. Chen, M. Ishaq, R. Tang, Z. Zheng, Z. Su, X. Li, X. Qiao, P. Fan, G. Liang, *Nano Energy* **2022**, *99*, 107417.

[34] J. Lin, G. Chen, N. Ahmad, M. Ishaq, S. Chen, Z. Su, P. Fan, X. Zhang, Y. Zhang, G. Liang, *J. Energy Chem.* **2023**, *80*, 256.

[35] M. Leng, M. Luo, C. Chen, S. Qin, J. Chen, J. Zhong, J. Tang, *Appl. Phys. Lett.* **2014**, *105*, 083905.

[36] C. N. Savory, D. O. Scanlon, *J. Mater. Chem. A* **2019**, *7*, 10739.

[37] G.-X. Liang, Y.-D. Luo, S. Chen, R. Tang, Z.-H. Zheng, X.-J. Li, X.-S. Liu, Y.-K. Liu, Y.-F. Li, X.-Y. Chen, Z.-H. Su, X.-H. Zhang, H.-L. Ma, P. Fan, *Nano Energy* **2020**, *73*, 104806.

[38] G. Liang, M. Chen, M. Ishaq, X. Li, R. Tang, Z. Zheng, Z. Su, P. Fan, X. Zhang, S. Chen, *Adv. Sci.* **2022**, *9*, 2105142.

[39] L. Guo, B. Zhang, S. Ranjit, J. Wall, S. Saurav, A. J. Hauser, G. Xing, L. Li, X. Qian, F. Yan, *Solar RRL* **2019**, *3*, 1900225.

[40] L. J. Phillips, C. N. Savory, O. S. Hutter, P. J. Yates, H. Shiel, S. Mariotti, L. Bowen, M. Birkett, K. Durose, D. O. Scanlon, J. D. Major, *IEEE J. Photovoltaics* **2019**, *9*, 544.

[41] R. E. Williams, Q. M. Ramasse, K. P. McKenna, L. J. Phillips, P. J. Yates, O. S. Hutter, K. Durose, J. D. Major, B. G. Mendis, *ACS Appl. Mater. Interfaces* **2020**, *12*, 21730.

[42] L. Wang, D.-B. Li, K. Li, C. Chen, H.-X. Deng, L. Gao, Y. Zhao, F. Jiang, L. Li, F. Huang, Y. He, H. Song, G. Niu, J. Tang, *Nat. Energy* **2017**, *2*, 17046.

[43] S. Wen, X. Yin, C. Zhang, Y. Guo, J. Liu, E. Wang, C. Zheng, W. Que, H. Liu, W. Liu, *Mater. Lett.* **2021**, *283*, 128770.

[44] S. Lu, H. Ding, J. Hu, Y. Liu, J. Zhu, R. Kondrotas, C. Chen, J. Tang, *Appl. Phys. Lett.* **2020**, *116*, 241602.

[45] N. Spalatu, R. Krautmann, A. Katerski, E. Karber, R. Josepson, J. Hiie, I. O. Acik, M. Krunks, *Sol. Energy Mater. Sol. Cells* **2021**, *225*, 111045.

[46] Y. Itzhaik, O. Niitsoo, M. Page, G. Hodes, *J. Phys. Chem. C* **2009**, *113*, 4254.

[47] K. Tsujimoto, D.-C. Nguyen, S. Ito, H. Nishino, H. Matsuyoshi, A. Konno, G. R. A. Kumara, K. Tennakone, *J. Phys. Chem. C* **2012**, *116*, 13465.

[48] Y. C. Choi, T. N. Mandal, W. S. Yang, Y. H. Lee, S. H. Im, J. H. Noh, S. I. Seok, *Angew. Chem. Int. Ed.* **2014**, *53*, 1329.

[49] M. Ishaq, S. Chen, U. Farooq, M. Azam, H. Deng, Z.-H. Su, Z.-H. Zheng, P. Fan, H.-S. Song, G.-X. Liang, *Solar RRL* **2020**, *4*, 2000551.

[50] Y. C. Choi, D. U. Lee, J. H. Noh, E. K. Kim, S. I. Seok, *Adv. Funct. Mater.* **2014**, *24*, 3587.

[51] C. Jiang, R. Tang, X. Wang, H. Ju, G. Chen, T. Chen, *Solar RRL* **2019**, *3*, 1800272.

[52] D. A. H. Hanaor, C. C. Sorrell, *J. Mater. Sci.* **2011**, *46*, 855.

[53] J. Han, X. Pu, H. Zhou, Q. Cao, S. Wang, Z. He, B. Gao, T. Li, J. Zhao, X. Li, *ACS Appl. Mater. Interfaces* **2020**, *12*, 44297.

[54] Y. Wang, R. Tang, L. Huang, C. Qian, W. Lian, C. Zhu, T. Chen, *ACS Appl. Mater. Interfaces* **2022**, *14*, 33181.

2300238 (14 of 15)

[55] W. Wang, L. Yao, J. Dong, L. Wu, Z. Cao, L. Hui, G. Chen, J. Luo, Y. Zhang, *Adv. Mater. Interfaces* **2022**, *9*, 2102464.

[56] S. Mariotti, O. S. Hutter, L. J. Phillips, P. J. Yates, B. Kundu, K. Durose, *ACS Appl. Mater. Interfaces* **2018**, *10*, 3750.

[57] O. S. Hutter, L. J. Phillips, K. Durose, J. D. Major, *Sol. Energy Mater. Sol. Cells* **2018**, *188*, 177.

[58] J. Major, L. Phillips, M. A. Turkestani, L. Bowen, T. Whittles, V. Dhanak, K. Durose, *Sol. Energy Mater. Sol. Cells* **2017**, *172*, 1.

[59] H. Shiel, O. S. Hutter, L. J. Phillips, J. E. N. Swallow, L. A. H. Jones, T. J. Featherstone, M. J. Smiles, P. K. Thakur, T.-L. Lee, V. R. Dhanak, J. D. Major, T. D. Veal, *ACS Appl. Energy Mater.* **2020**, *3*, 11617.

[60] J. E. N. Swallow, B. A. D. Williamson, T. J. Whittles, M. Birkett, T. J. Featherstone, N. Peng, A. Abbott, M. Farnworth, K. J. Cheetham, P. Warren, D. O. Scanlon, V. R. Dhanak, T. D. Veal, *Adv. Funct. Mater.* **2018**, *28*, 1701900.

[61] G. Kresse, J. Hafner, *Phys. Rev. B* **1993**, *47*, 558.

[62] G. Kresse, J. Hafner, *Phys. Rev. B* **1994**, *49*, 14251.

[63] G. Kresse, J. Furthmüller, *Phys. Rev. B* **1996**, *54*, 11169.

[64] G. Kresse, J. Furthmüller, *Comput. Mater. Sci.* **1996**, *6*, 15.

[65] A. V. Krukau, O. A. Vydrov, A. F. Izmaylov, G. E. Scuseria, *J. Chem. Phys.* **2006**, *125*, 224106.

[66] P. E. Blöchl, *Phys. Rev. B* **1994**, *50*, 17953.

[67] M. Einhorn, B. A. D. Williamson, D. O. Scanlon, *J. Mater. Chem. A* **2020**, *8*, 7914.

[68] B. A. Williamson, G. J. Limburn, G. W. Watson, G. Hyett, D. O. Scanlon, *Matter* **2020**, *3*, 759.

[69] P. Hartley, R. G. Egdell, K. H. L. Zhang, M. V. Hohmann, L. F. J. Piper, D. J. Morgan, D. O. Scanlon, B. A. D. Williamson, A. Regoutz, *J. Phys. Chem. C* **2021**, *125*, 6387.

[70] A. G. Squires, D. O. Scanlon, B. J. Morgan, *Chem. Mater.* **2020**, *32*, 1876.

[71] D. O. Scanlon, C. W. Dunnill, J. Buckeridge, S. A. Shevlin, A. J. Logsdail, S. M. Woodley, C. R. A. Catlow, M. J. Powell, R. G. Palgrave, I. P. Parkin, G. W. Watson, T. W. Keal, P. Sherwood, A. Walsh, A. A. Sokol, *Nat. Mater.* **2013**, *12*, 798.

[72] B. A. D. Williamson, J. Buckeridge, N. P. Chadwick, S. Sathasivam, C. J. Carmalt, I. P. Parkin, D. O. Scanlon, *Chem. Mater.* **2019**, *31*, 2577.

[73] M. Quesada-Gonzalez, B. A. D. Williamson, C. Sotelo-Vazquez, A. Kafizas, N. D. Boscher, R. Quesada-Cabrera, D. O. Scanlon, C. J. Carmalt, I. P. Parkin, *J. Phys. Chem. C* **2018**, *122*, 714.

[74] A. M. Alotaibi, S. Sathasivam, B. A. D. Williamson, A. Kafizas, C. Sotelo-Vazquez, A. Taylor, D. O. Scanlon, I. P. Parkin, *Chem. Mater.* **2018**, *30*, 1353.

[75] R. Krautmann, N. Spalatu, R. Gunder, D. Abou-Ras, T. Unold, S. Schorr, M. Krunks, I. Oja Acik, *Solar Energy* **2021**, *225*, 494.

[76] A. Walsh, D. J. Payne, R. G. Egdell, G. W. Watson, *Chem. Soc. Rev.* **2011**, *40*, 4455.

[77] J. J. Carey, J. P. Allen, D. O. Scanlon, G. W. Watson, *J. Solid State Chem.* **2014**, *213*, 116.

[78] C. H. Don, H. Shiel, T. D. C. Hobson, C. N. Savory, J. E. N. Swallow, M. J. Smiles, L. A. H. Jones, T. J. Featherstone, P. K. Thakur, T.-L. Lee, K. Durose, J. D. Major, V. R. Dhanak, D. O. Scanlon, T. D. Veal, *J. Mater. Chem. C* **2020**, *8*, 12615.

[79] T. Hobson, K. Durose, *Mater. Sci. Semicond. Process.* **2021**, *127*, 105691.

[80] T. J. Nagle, A. R. Davies, J. R. Sites, *MRS Online Proc. Libr.* **2007**, *1012*, 1203.

[81] N. Naghavi, S. Temgoua, T. Hildebrandt, J. F. Guillemoles, D. Lincot, *Prog. Photovoltaics Res. Appl.* **2015**, *23*, 1820.

[82] X. Li, K. Shen, Q. Li, Y. Deng, P. Zhu, D. Wang, *Solar Energy* **2018**, *165*, 27.

[83] R. Saive, *IEEE J. Photovoltaics* **2019**, *9*, 1477.

[84] D. Pjević, M. Obradović, T. Marinković, A. Grce, M. Milosavljević, R. Grieseler, T. Kups, M. Wilke, P. Schaaf, *Physica B* **2015**, *463*, 20.

[85] L. S. Hsu, R. Rujkorakarn, J. R. Sites, C. Y. She, *J. Appl. Phys.* **1986**, *59*, 3475.

[86] S.-T. Zhang, H. Roussel, O. Chaix-Pluchery, M. Langlet, D. Muñoz-Rojas, D. Bellet, A. Klein, *J. Phys. Chem. C* **2017**, *121*, 17305.

[87] J. Zhang, M. Li, Z. Feng, J. Chen, C. Li, *J. Phys. Chem. B* **2006**, *110*, 927.

[88] A. Kanevce, M. Gloeckler, A. O. Pudov, J. R. Sites, *MRS Online Proc. Libr.* **2005**, *865*, 532.

[89] A. C. Breeson, G. Sankar, G. K. Goh, R. G. Palgrave, *Appl. Surf. Sci.* **2017**, *423*, 205.

[90] D. Koch, S. Manzhos, *J. Phys. Chem. Lett* **2017**, *8*, 1593.

[91] J. Muscat, N. M. Harrison, G. Thornton, *Phys. Rev. B* **1999**, *59*, 2320.

[92] N. A. Deskins, R. Rousseau, M. Dupuis, *J. Phys. Chem. C* **2010**, *114*, 5891.

[93] P. Lindan, N. Harrison, J. Holender, M. Gillan, M. Payne, *Surf. Sci.* **1996**, *364*, 3431.

[94] J. C. Woicik, E. J. Nelson, L. Kronik, M. Jain, J. R. Chelikowsky, D. Heskett, L. E. Berman, G. S. Herman, *Phys. Rev. Lett.* **2002**, *89*, 077401.

[95] A. G. Thomas, W. R. Flavell, A. K. Mallick, A. R. Kumarasinghe, D. Tsoutsou, N. Khan, C. Chatwin, S. Rayner, G. C. Smith, R. L. Stockbauer, S. Warren, T. K. Johal, S. Patel, D. Holland, A. Taleb, F. Wiame, *Phys. Rev. B* **2007**, *75*, 035105.

[96] J. Scofield, *J. Electron. Spectrosc. Relat. Phenom.* **1976**, *8*, 129.

[97] J. Yeh, I. Lindau, *At. Data Nucl. Data Tables* **1985**, *32*, 1.

[98] A. Regoutz, F. Oropeza, C. Poll, D. Payne, R. Palgrave, G. Panaccione, F. Borgatti, S. Agrestini, Y. Utsumi, K. Tsuei, Y. Liao, G. Watson, R. Egdell, *Chem. Phys. Lett.* **2016**, *647*, 59.

[99] A. Regoutz, M. Mascheck, T. Wiell, S. K. Eriksson, C. Liljenberg, K. Tetzner, B. A. D. Williamson, D. O. Scanlon, P. Palmgren, *Rev. Sci. Instrum.* **2018**, *89*, 073105.

[100] W. Wang, Z. Cao, H. Wang, J. Luo, Y. Zhang, *J. Mater. Chem. A* **2021**, *9*, 26963.

[101] V. Pfeifer, P. Erhart, S. Li, K. Rachut, J. Morasch, J. Brötz, P. Reckers, T. Mayer, S. Rühle, A. Zaban, I. Mora Seró, J. Bisquert, W. Jaegermann, A. Klein, *J. Phys. Chem. Lett.* **2013**, *4*, 4182.

[102] Y. Mi, Y. Weng, *Sci. Rep.* **2015**, *5*, 11482.

[103] Y. Nosaka, A. Y. Nosaka, *J. Phys. Chem. Lett.* **2016**, *7*, 431.

[104] P. Yan, X. Wang, X. Zheng, R. Li, J. Han, J. Shi, A. Li, Y. Gan, C. Li, *Nano Energy* **2015**, *15*, 406.

[105] X. Wang, S. Shen, Z. Feng, C. Li, *Chin. J. Catal.* **2016**, *37*, 122059.

[106] A. Li, Z. Wang, H. Yin, S. Wang, P. Yan, B. Huang, X. Wang, R. Li, X. Zong, H. Han, C. Li, *Chem. Sci.* **2016**, *7*, 6076.

[107] Y. Zhu, K. Deng, H. Sun, B. Gu, H. Lu, F. Cao, J. Xiong, L. Li, *Adv. Sci.* **2018**, *5*, 1700614.

[108] R. Scheer, H.-W. Schock, in *Chalcogenide Photovoltaics: Physics, Technologies, and Thin Film Devices*, Wiley–VCH, Weinheim, Germany **2011**.

[109] M. Gloeckler, C. Jenkins, J. R. Sites, *MRS Proc.* **2003**, *763*, B520.

[110] G. T. Koishiyev, J. R. Sites, 2009 34th IEEE Photovoltaic Spec. Conf. (PVSC), Philadelphia, PA, USA **2009**, 001978.

[111] Y. Li, J. K. Cooper, W. Liu, C. M. Sutter-Fella, M. Amani, J. W. Beeman, A. Javey, J. W. Ager, Y. Liu, F. M. Toma, I. D. Sharp, *Nat. Commun.* **2016**, *7*, 12446.

[112] S. Hegedus, *IEEE Trans. Electron Devices* **1984**, *31*, 629.

[113] M. Gloeckler, J. R. Sites, *J. Appl. Phys.* **2004**, *95*, 4438.

[114] F. Liu, C. Yan, K. Sun, F. Zhou, X. Hao, M. A. Green, *ACS Photonics* **2017**, *4*, 1684.